

Impact of Tab Location on Large Format Lithium-Ion Pouch Cell Based on Fully Coupled Tree-Dimensional Electrochemical-Thermal Modeling



Ahmadou Samba^{a,b,*}, Noshin Omar^a, Hamid Gualous^b, Odile Capron^a, Peter Van den Bossche^a, Joeri Van Mierlo^a

^a MOBI, Vrije Universiteit Brussel, Pleinlaan 2, Brussel, 1050, Belgium

^b LUSAC, Université de Caen Basse Normandie, Rue Louis Aragon, 50130 Cherbourg, France

ARTICLE INFO

Article history:

Received 13 June 2014

Received in revised form 26 August 2014

Accepted 30 August 2014

Available online 30 September 2014

Keywords:

Li-ion battery

tab design

3D electrochemical-thermal modeling

Finite Element Method (FEM)

Distributions

ABSTRACT

This paper presents extensive three-dimensional (3D) simulations of large LiFePO₄ pouch cells. 3D simulations of the Li-ion battery behavior are highly nonlinear and computationally demanding. Coupling electrochemical modeling to thermal models represents an important step towards accurate simulation of the Li-ion battery. Non-uniform temperature, potential and current density through the battery induce non-uniform use of the active material and can have a negative impact on cell performance and lifetime. Different pouch cell designs, with different tab locations, have been investigated in term of performance, current density, potential and heat distributions. The model is first validated with experimental data at different current discharge rates. Afterwards, the electrochemical, thermal and electrical behaviors over each cell design under high discharge rate (4 I_c) are compared between configurations. It has been shown that the designs with symmetrical configurations show uniform potential and current density gradient, which minimize the ohmic heat and lead to more uniform active material utilization and temperature distributions across the cell surface.

© 2014 Elsevier Ltd. All rights reserved.

1. Introduction

Lithium-ion batteries have emerged as key energy storage devices, and are now the main technology for portable devices. Due to their high potential and their high energy and power densities, and also their good lifetime, they are now the preferred battery technology for Hybrid Electric Vehicles (HEVs), Battery Electric Vehicles (BEVs) and Plug-In Hybrid Electric Vehicles (PHEVs) [1–3].

Advanced research in this field enables wide use of large-format, high-capacity Li-ion pouch cells in PHEVs and EVs. This format has the advantage of reducing the number of cells in the module, increasing the capacity and reducing the size and weight at pack level. Increasing the current amplitude during the charge/discharge process subjects the large format battery to abuse situations and leads to non-uniform distributions of temperature, potential, current density and heat generation through the cell. These phenomena may reduce battery performance and lifetime [4–6], leading to thermal runaway in worst cases [7–9] and

requiring a more complex cooling strategy. Based on this observation, the main barriers to their wide use are the need for fast charging (using high current rate), and the need for BEVs to perform high acceleration (resulting in high discharge rate). Therefore, good cell design is necessary to avoid non-uniform distribution of the electrical and thermal parameters. Particle size and electrode coating thickness also have a significant impact on battery behavior. Recently, Zhao et al [10] showed that small coin cells provide much better performance and energy density than large format cells, where uneven current density is observed, leading to lower utilization of the active material. In addition, the impact of the arrangements and number of the current collecting tabs are investigated in the cases of wound design [10,11] and stacked layer design [12,13]. As a function of the number and location of tabs, the electron pathways become more or less long and thereby cause an increase or decrease of the ohmic resistance responsible for the voltage loss. In order to investigate these battery designs, electrochemical modeling techniques are more appropriate than electrical modelling because they show a clear relation between the electrochemical parameters and battery geometry. Several 1D electrochemical models are listed in the literature [14–17]. These are more suitable for describing small-format battery behavior. They also provide average values for large-format

* Corresponding author. Tel.: +32 255 915 12.

E-mail addresses: ahmadou.samba@vub.ac.be, ahmadou.samba@gmail.com (A. Samba).

Nomenclature

A_{tab}	Cross section of the tab (m^2)
c_1	Concentration of lithium in the active material particles (mol/m^3)
c_2	Concentration of lithium in the electrolyte (mol/m^3)
C_{dl}	Electrical double layer capacitance, (F/m^2)
C_p	Thermal capacitance ($J/kg.K$)
D_1	Diffusion coefficient of lithium in the solid phase (m^2/s)
D_2	Diffusion coefficient of lithium in the electrolyte (m^2/s)
$Ea_{D_s,j}$	Activation energy for particle diffusion [J/mol]
$Ea_{R,j}$	Activation energy for reaction [J/mol]
f_{\pm}	Average molar activity coefficient
F	Faraday's constant (C/mol)
h	Convective heat transfer coefficient (W/m^2K)
i_1	Electronic current density in the solid phase
i_2	Ionic current density in the liquid phase
i_N	Normal inward current density through the electrode/CC interfaces (A/m^2)
i_{app}	Total applied current density (A)
J_0	Exchanged current density (A/m^2)
J_n	Local charge transfer current density (A/m^2)
k_0	Reaction rate constant ($m^{2.5}/mol^{0.5} s$)
L_{PCC}	Positive current collector thickness (m)
L_P	Positive electrode thickness (m)
L_S	Separator thickness (m)
L_{NE}	Negative electrode thickness (m)
L_{NCC}	Negative current collector thickness (m)
N	Total number of single cell
r	Radius distance variable of the solid particles (m)
R	Gas constant, 8.314 ($J/mol.K$)
R_s	Radius of electrode particle (m)
S_a	Specific surface area (m^{-1})
t	Time (s)
t_+	Transferring number of Li^+
T	Absolute temperature (K)

Greek letters

ε_2	Electrolyte volume fraction
ε_1	Active material volume fraction
Φ_1	Solid phase potential (V)
Φ_2	liquid phase potential (V)
Φ_{cc}	Current collector potential (V)
α	Charge transfer coefficient
γ	Bruggeman tortuosity exponent
η	Local surface overpotential (V)
σ_1	Electronic conductivity of solid matrix (S/m)
σ_2	Ionic conductivity of electrolyte (S/m)
ρ	Density (kg/m^3)
λ	Thermal conductivity ($W/m.K$)

Subscripts, superscripts and acronyms

0	Initial value
1	Solid phase
2	Liquid phase
p	positive
n	negative
eff	Effective value
CC	Current collector
ref	Reference value
j	Indice of the electrodes
surf	surface

max	maximum
amb	ambient
rea	reaction
ohm	ohmic
act	activation
s	solid
l	liquid
PE	Positive electrode
NE	Negative electrode
SP	Separator
SOC	State of charge
DOD	Depth of discharge

batteries without taking into account the collector tabs. However, they are not sufficient to handle the issue of non-uniform thermal, electrical and electrochemical variable distributions observed in large-format cells. Recent advances in numerical simulation techniques applied to Li-ion batteries have given more attention to the development of 2D axisymmetric and 3D electrochemical-thermal modeling [10,11,18–20]. The multi-dimensional simulations are highly nonlinear and computationally demanding, and coupling electrochemical and thermal modeling represents an important step towards accurate simulation of the Li-ion battery. Most of the 2D and 3D electrochemical-thermal models are applied to the spirally wound design in order to gain insight into large-scale battery behavior and also to investigate the impact of the number of collecting tabs on battery performance. However, little work is focused on stacked layered designs and the impact of their tab positioning on performance and variable distributions. This paper presents an extensive fully coupled three-dimensional (3D) simulation of electrochemical-thermal modeling describing the behavior of large $LiFePO_4$ pouch cells. Different pouch cell designs with various tab locations have been investigated in terms of performance and distribution. The model is first validated with experimental data at different discharging current rates. Afterwards, the electrochemical, thermal and electrical behaviors of each cell design under high discharge rate ($4 I_L$) are compared in order to select the best configuration. Finally, the impact of tab width on the temperature, potential and current density distributions are also investigated in depth.

2. Model Description

2.1. Model assumptions and geometry features

A 3D electrochemical-thermal modeling is developed for a high-energy $LiFePO_4$ /carbon pouch cell, manufactured by European Batteries. As it is well-known, the battery is composed of several layers. Since the modeling of all layers required a lot of meshing effort and then long computational times. 1D electrochemical coupled with the thermal model applied on a single cell layer has been used in several works [21–24]. The model was validated by comparing simulation to the experimental test performed on the whole battery. Therefore a single electrode plate pair approach can be modeled to describe the pouch cell behaviors. The single electrode cell used is assumed to be a stack layered design and composed of both collectors (positive and negative) with collecting tabs, the positive electrode (PE), the separator and the negative electrode (NE). The whole is bathed in the electrolyte (2 mol/L $LiPF_6$ in EC/DMC solvent) as illustrated in Fig. 1. The geometrical details such as the electrodes, separator and current collectors, tabs thicknesses and particle radius are included in Table 4. Several designs of single

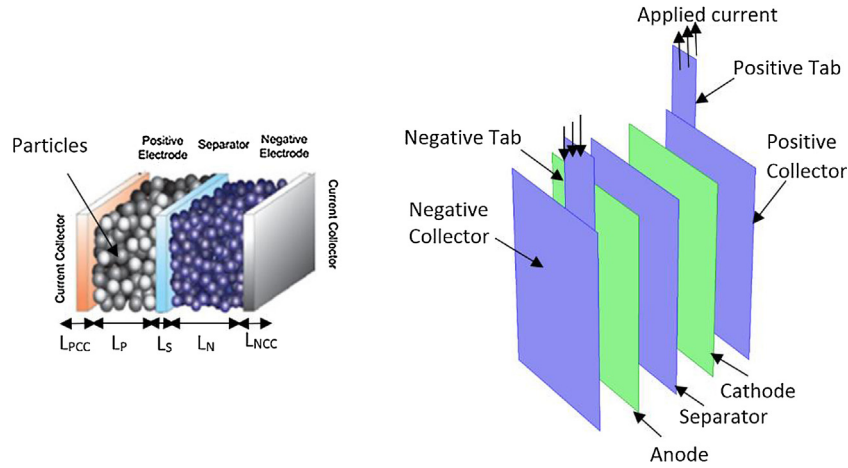


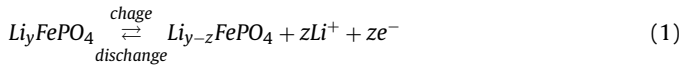
Fig. 1. single electrode plate pair configuration and components thicknesses.

electrode configuration are investigated, where the collecting tab positioning changes as shown in Fig. 2.

2.2. Electrochemical modeling

The electrochemical process during discharge is mainly represented by energy conversion from the chemical to the electrical, and during charge the inverse process occurs. These conversions occur at the solid electrolyte interface (SEI) by mean of electrochemical reactions as described below:

At the positive electrode:



At the negative electrode:



In the charge process, lithium ions are deintercalated from the cathode material and an equal number of lithium ions and electrons are produced. Then the lithium ions migrate through the electrolyte where they are intercalated into the anode. Each passage of a lithium ion into the internal circuit of the battery is compensated by the passing of an electron through the collectors because the electrons cannot cross through the separator. These processes are exothermic due to the ohmic losses, activation losses, and other irreversible processes. According to the above physical description, lithium-ion batteries are modeled using porous electrode theory coupled with various transport and reaction mechanisms. This

theory determines the concentration of lithium ions, the potential in the electrolyte and in the intercalation particles, as well as in the collectors and tabs. The electrochemical reaction kinetics for lithium-ion intercalation/deintercalation at the SEI is also estimated. As the physical parameters depend on the cell temperature, the porous electrode theory is coupled with the energy balance. All the required variables are listed in Table 1.

The battery cell is divided into several geometrical domains. Each corresponds to a particular physical length scale as described in Fig. 1. The dynamic performance of a lithium-ion cell is characterized by the solution of the electrochemically and thermally coupled equations as summarized in Table 2.

The electrodes are assumed to be porous material consisting of a lattice of several spherical particles (with ε_s the corresponding volume fraction) immersed in the electrolyte (with ε_l the corresponding volume fraction). The electrochemical processes and transport phenomena in the porous electrode and particles are described by an extended 3D porous electrode model derived from the work of Newman et al. [14]. The intercalated lithium concentration in the spherical particle is computed from the mass balance (Fick's second law), as shown in Eq. (3). Due to symmetry, the lithium flux is equal to zero at the center of the particle, while at the surface of the particle (SEI), the lithium flux is equal to the surface electrochemical reaction rate (J_j). Furthermore, the lithium-ion transport in the electrolyte phase is modeled by using the concentrated solution theory as shown in Eq. (4), where the flux is equal to zero (no reaction) at the electrode/collector interfaces; additionally there is continuity of species flux in the electrolyte at the electrode/separators interfaces. At the SEI, the surface electrochemical reaction rate is represented by the Butler-Volmer equation as shown in Eq. (7). The

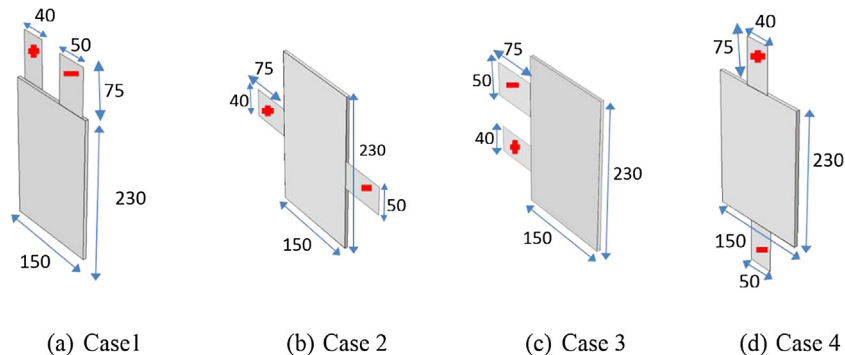


Fig. 2. different designs and dimensions (mm) of pouch cell.

Table 1
variables of the model.

Domain	Variable name	Symbol	SI Unity	variable
Particle	Li concentration in solid phase	$c_{1,j}(j = p, n)$	mol.m^{-3}	t, r, x, y, z
PorousElectrode		c_2		t, x, y, z
	Li+ concentration in electrolyte	Φ_2	mol.m^{-3}	
	Potential in solution phase	Φ_1	V	
	Potential in solid phase	$J_j(j = p, n)$	V	
	Surface reaction rate		$\text{mol.m}^{-2}.\text{s}^{-1}$	
Cell	Temperature	T	K	t, x, y, z
	potential in collector& Tabs	$\Phi_{cc,j}(j = p, n)$	V	

transport and kinetic parameters are dependent on the exchange current density, the overpotential and temperature variation of the system. The potential in the solid phase is derived from the charge balance governed by Ohm's law as described by Eq. (5). At the electrode/separator interfaces there is no flux of charge (the separator acts as a barrier for the passage of the electrons), while at the electrode/collector interfaces the charge flux corresponds to the total current in the circuit. The potential in the electrolyte phase is also governed by Ohm's law, defined as a function of reaction current density and the local concentration of lithium, as shown in Eq. (6), where at the electrode/collector interfaces the potential gradient is equal to zero. A continuity of charge flux is considered in the electrolyte at the electrode/separator interfaces.

The governing equations for the charge balance in the collectors are given by Eq. (8), where no transverse current is flowing through the tab domains. The current density is applied at the top cross-section of the positive tab, while the potential at the top of the negative tab is fixed at zero.

2.3. Thermal modeling

The electrochemical model is coupled to the thermal model in order to estimate the cell temperature change. Taking into account the small thickness (13 mm) of the pouch cell used in this study, the temperature gradient across the cell thickness is generally negligible. Thus a two-dimensional transient model can be used, as discussed in [25]. Therefore a pouch cell can be modeled with a single cell sandwich, which can be likened to a 2D cell. From this assumption, the heat equation is solved in the same geometry as used in the electrochemical model to ensure better spatial coupling of the se two physics. As shown in Eq. (9), the energy balance is solved at each layer (electrodes, separator and current collectors and tabs included). Heat generation is mainly composed of the contributions of polarization heat, ohmic heat and reversible heat as expressed in Eq. (10)–(12). At the interfaces between cell components (current collectors/electrodes and electrodes/separator), the continuity of the heat flux is applied as an internal boundary

Table 2
Governing equation and boundaries conditions[14].

Physics	Governing equations and boundaries conditions	Eq. Number
Mass balance in solid phase	$\frac{\partial c_{1,j}}{\partial t} = \nabla \cdot (D_{1,j} \nabla c_{1,j})$ $-\nabla \cdot c_{1,j} _{r=0} = 0; -D_{1,j} \nabla c_{1,j} _{r=R_{s,j}} = \frac{J_{n,j}}{S_{a,j}F}; (j = p, n)$	(3)
Mass balance in electrolyte phase	$\varepsilon_2 \frac{\partial c_2}{\partial t} = \nabla \cdot (D_2^{eff} \nabla c_2) + \frac{S_{a,j} J_{n,j}}{F} (1 - t_+); D_2^{eff} = D_2 \varepsilon_2^2$ $-\nabla \cdot c_2 _{NE/CC^- \text{ and } PE/CC^+}^{interfaces} = 0; -\nabla \cdot c_2 _{PE/SP}^{interfaces} = -\nabla \cdot c_2 _{NE/SP}^{interfaces}$	(4)
Electron transport in the solid phase	$\nabla \cdot i_1 = -S_{a,j} \left(J_{n,j} + C_{dl} \left(\frac{\partial \Phi_1}{\partial t} - \frac{\partial \Phi_2}{\partial t} \right) \right);$ $i_1 = -\sigma_1^{eff} \nabla \Phi_1; \sigma_1^{eff} = \sigma_1 \varepsilon_1^2; S_{a,j} = \frac{3\varepsilon_{1,j}}{R_{s,j}}$ $-\sigma_1^{eff} \nabla \cdot \Phi_1 _{NE/CC^+}^{interfaces} = i_{N,j}; -\sigma_1^{eff} \nabla \cdot \Phi_1 _{NE/SP \text{ and } PE/SP}^{interfaces} = 0; (j = p, n)$	(5)
Ionic transport in the solution phase	$\nabla \cdot i_2 = S_{a,j} J_{n,j}$ $i_2 = -\sigma_2^{eff} \nabla \Phi_2 + \frac{2RT\sigma_2^{eff}}{F} (1 - t_+) \left(1 + \frac{d \ln f_{\pm}}{d \ln c_2} \right) \nabla \ln c_2$	(6)
Electrochemical kinetics	$\nabla \cdot \Phi_2 _{NE/CC^- \text{ and } PE/CC^+}^{interfaces}$ $J_{n,j} = J_{0,j} \left[\exp \left(\frac{\alpha_a F}{RT} \eta_j \right) - \exp \left(\frac{\alpha_c F}{RT} \eta_j \right) \right]; J_{0,j} = F k_{0,j} c_2^{\alpha_a} (c_{1,j,max} - c_{1,j,surf})^{\alpha_a} c_{1,j,surf}^{\alpha_c}$ $\eta_j = \Phi_1 - \Phi_2 - U_j; c_{1,j,surf} = c_{1,j} _{r=R_s}$	(7)
Potential in collectors & Tabs	$\nabla \cdot (-\sigma_{cc,j} \nabla \Phi_{cc,j}) = -i_{N,j} \text{ at the PE/CC and NE/CC}$ $i_{N,j} = 0 \text{ at the tabs}$ $n \cdot (-\sigma_{cc,j} \nabla \Phi_{cc,j}) = i_{app,j} = \frac{I_{app}}{N \cdot A_{tab}} \text{ at top of the tab}$ $\Phi_{cc,n} = 0 (j = n) \text{ at the top of the negative tab}$	(8)
Energy balance	$\rho_j c_{p,j} \frac{dT}{dt} - \lambda_j \nabla^2 T = q_{rea,j} + q_{act,j} + q_{ohm,j}$ $\lambda_j \Delta T _{CC \text{ and } Tabs/ambient} = h(T - T_a)$	(9)
reversible heat	$q_{rea,j} = S_{a,j} J_{n,j} \left(T \frac{dU_j}{dT} \right)$	(10)
polarization heat	$q_{act,j} = S_{a,j} J_{n,j} \eta_j$	(11)
Ohmic heat	$q_{ohm} = -i_1 \nabla \cdot \Phi_1 - i_2 \nabla \cdot \Phi_2 - i_{cc,j} \nabla \cdot \Phi_{cc,j}; (j = p, n)$	(12)

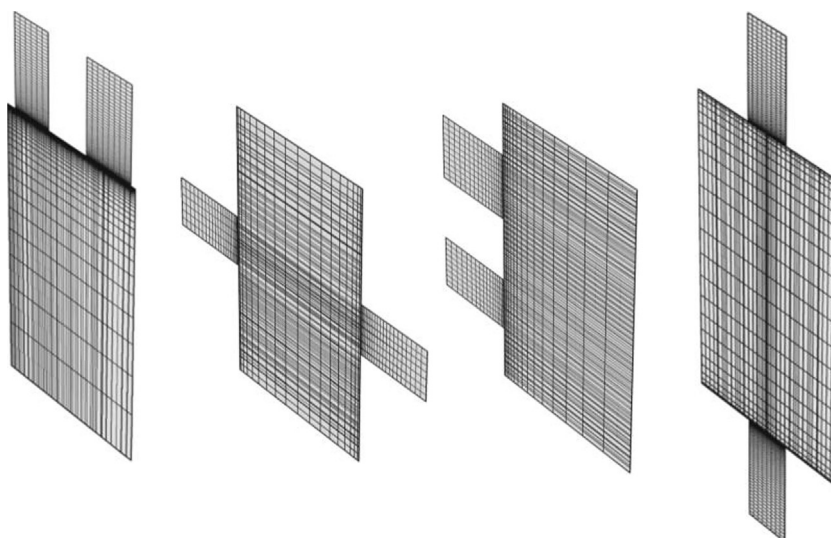


Fig. 3. Meshing of different cell designs.

condition. Furthermore, to match the experimental conditions, model validation is conducted by taking into account convective heat transfer. Convective heat transfer is calculated using the methodology as described in [25] and included in Table 4. Afterwards, the model is performed in adiabatic conditions in order to compare the performances and behaviors of the different cell designs.

2.4. Model Input

The effective parameters are obtained by multiplying the porosity (ε_j) power to the tortuosity (γ_j , Bruggeman coefficient) of the porous electrode. In addition, electrochemical parameters such as the diffusion coefficient of lithium in the solution and solid phases, the ionic electrical conductivity of the solution phase, the open circuit potential, the entropy coefficient and the reaction rate are affected by temperature change through the Arrhenius law and other empirical relations, as listed in Table 3.

To compute this model, the dimensions of the different components as well as the electrochemical and thermal parameters are needed. The used input data come from the literature and are listed in Table 4.

2.5. Numerical method and Validation

2.5.1. Numerical aspects

All equations are simultaneously solved numerically in COMSOL Multiphysics 4.3b with the Batteries and Fuel cells toolbox by using the Finite Elements Method (FEM). As the governing equations are highly nonlinear, the performance and accuracy of the calculation depends heavily on the mesh and solver. A hexahedral mesh is used, generated from the swept method. To ensure the accuracy and the mesh independency of the solutions, 16,700 hexahedral elements are used over the entire computational domain after testing several grid densities with refining zones at each component thickness, especially at the electrolyte and also at the junction between the tab and the current collector, as illustrated in Fig. 3. In order to save memory and time, the equations are coupled by using the segregated approach as shown in Fig. 4. At each time step, two segregated steps are considered: first, the temperature is solved by keeping the electrochemical variables constant, and second, the results of temperatures at each mesh nodes are used to update the

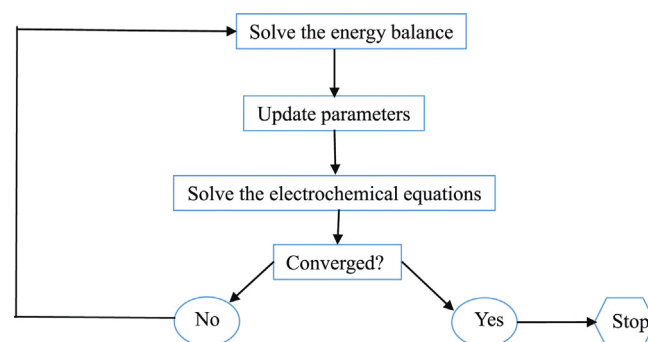


Fig. 4. Procedure of the numerical solution at each time step.

corresponding local electrochemical parameters and then the local electrochemical variables of each mesh nodes are calculated. The process is repeated at each node until the convergence is reached for all variables. The direct solver PARDISO (Parallel Direct Sparse Solver Interface) was chosen as linear solver. For each time step, the convergence is reached where the relative tolerance is below than 10^{-3} for all variables. Then, the time step progresses until the cut-off potential is reached.

2.5.2. Model validation

Different capacity tests were carried out at various discharge current rates ($1I_t$, $2I_t$, $3I_t$ and $4I_t$) under 20°C of ambient and initial temperatures. I_t stands for the current value corresponding to the battery capacity in Ah as defined in IEC61434. A commercial LiFePO_4 /carbon high-energy pouch cell manufactured by European Batteries, with the design of case 1, is used. The electrode dimensions are presented both in Fig. 2 and in Table 4. During the capacity test the cell was cycled between 0%–80% DoD. The maximum and minimum cell potential are 3.65 V and 2 V, respectively. The PEC Corporation SBT 0550 battery tester system was used to monitor the current, potential and temperature. 9 thermocouples ($75\ \mu\text{m}$, K-type) were placed on the upper side of the battery surface as illustrated in the work of Samba et al. [25] with the accuracy of $\pm 0.1^\circ\text{C}$ obtained from [26].

The sandwich structure can be considered as a parallel circuit. The single cell potentials are almost the same. The total current is almost equal to the sum of the currents in each single cell. From

Table 3
temperature dependency of parameters [18,28].

Parameters	Equations	Eq. Number
Diffusion coefficient of the solid phase	$D_{1,j} = D_{1,j,ref} \exp \left[-\frac{E_{aD1,j}}{R} \left(\frac{1}{T} - \frac{1}{T_{ref}} \right) \right]; (j = p, n)$	(13)
Diffusion coefficient of the liquid phase	$D_{2,j} = 10^{-4.43 - \left(\frac{54}{T - 229 - 0.005c_2} \right) - 4}$	(14)
The reaction rate	$k_{0,j} = k_{0,j,ref} \exp \left[-\frac{E_{aR}}{R} \left(\frac{1}{T_{ref}} - \frac{1}{T} \right) \right]; (j = p, n)$	(15)
The ionic conductivity	$\sigma_2 = 10^{-4} c_2 \times 1.2544$ $\left(-8.2488 + 0.053248T - 0.00002987T^2 + 0.26235 \times 0.001c_2 - 0.0093063 \right.$ $\left. \times 0.001c_2T + 0.000008069 \times 0.001c_2T^2 + 0.22002 \times 10^{-6}c_2^2 - 0.0001765 \times 10^{-6}c_2^2T \right)^2$	(16)
Open circuit potential	$U_j = U_{ref,j} + (T - T_{ref}) \frac{dU_j}{dT}$ $U_{ref,p} = 3.4323 - 0.4828 \exp \left(-80.2493 (1 - \theta_p)^{1.3198} \right) - 3.2474$ $\times 10^{-6} \exp \left(-20.2645 (1 - \theta_p)^{3.8003} \right) + 3.2482$ $\times 10^{-6} \exp \left(-20.2646 (1 - \theta_p)^{3.7995} \right)$ $U_{ref,n} = 0.6379 + 0.5416 \exp \left(-305.5309 \theta_n \right)$ $+ 0.044 \tanh \left[\frac{-\theta_n - 0.1958}{0.1088} \right] - 0.1978 \tanh \left[\frac{\theta_n - 1.0571}{0.0854} \right]$ $- 0.6875 \tanh \left[\frac{\theta_n + 0.0117}{0.0529} \right] - 0.0175 \tanh \left[\frac{\theta_n - 0.5692}{0.0875} \right]$ $\theta_j = \frac{c_{2,j}}{c_{2,j,max}}; (j = p, n)$ State of charge (SOC) $\frac{dU_p}{dT} = -0.35376 \theta_p^8 + 1.3902 \theta_p^7 - 2.2585 \theta_p^6 + 1.9635 \theta_p^5$ $- 0.98716 \theta_p^4 + 0.28857 \theta_p^3 - 0.046272 \theta_p^2 + 0.0032158 \theta_p - 1.9186$ $\frac{dU_n}{dT} = -344.1347148 \times \frac{\exp(-32.9633287 \theta_n + 8.316711484)}{1 + 749.0756003 \exp(-34.79099646 \theta_n + 8.887143624)}$ $- 0.8520278805 \theta_n + 0.362299229 \theta_n^2 + 0.2698001697$	(17)
Entropy coefficient	$\frac{dU_p}{dT} = -0.35376 \theta_p^8 + 1.3902 \theta_p^7 - 2.2585 \theta_p^6 + 1.9635 \theta_p^5$ $- 0.98716 \theta_p^4 + 0.28857 \theta_p^3 - 0.046272 \theta_p^2 + 0.0032158 \theta_p - 1.9186$ $\frac{dU_n}{dT} = -344.1347148 \times \frac{\exp(-32.9633287 \theta_n + 8.316711484)}{1 + 749.0756003 \exp(-34.79099646 \theta_n + 8.887143624)}$ $- 0.8520278805 \theta_n + 0.362299229 \theta_n^2 + 0.2698001697$	(18)

this reason, we downscaled the current by taking into account the current passing through representing other layers. As the capacity of the pouch cell is 45Ah, a single electrode plate pair is modeled with a capacity of (C =Capacity of the entire cell/total number of electrode pair (N)), where N is 77, therefore the capacity used in the model is 0.58Ah and the applied current density is equal to

$$\left(i_{app} = \frac{I_t}{N * \text{positive tab cross-section}} \right) \quad (19)$$

The initial electrochemical parameters (concentration and potential in electrolyte and solid particle, state of charge) are obtained from model calibration. The model is validated by

comparing the experimental temperature given by the thermocouples and the measured potential with the model results.

In Fig. 5, the cell potentials from the simulations are compared with the experimental results at different constant discharge current rates, the cell potential was computed from the difference between the positive tab and the negative tab potentials. A good agreement is shown between the model and experimental data, except at the end of the discharge, where a difference is noticeable, and this difference may result from the inaccuracy of the electrochemical parameters used, which did not take into account the battery lifespan. In the work of Samba et al. [25], the temperature distribution over the battery surface has been shown to be nearly

Table 4
Input parameters for a 45 Ah LiFePO₄ energy battery [18,28].

Parameters	Symbol	Cu foil	Anode	Separator	Cathode	Al foil
Thickness	$l_j [m]$	$2 \cdot 10^{-5}$	$3.4 \cdot 10^{-5}$	$2.5 \cdot 10^{-5}$	$8 \cdot 10^{-5}$	$1 \cdot 10^{-5}$
Particle radius	$R_{s,j,ref} [m]$	-	$14.75 \cdot 10^{-6}$	-	$1.15 \cdot 10^{-6}$	-
Active material volume fraction	$\varepsilon_1 [l]$	-	0.56	-	0.435	-
Porosity	$\varepsilon_2 [l]$	-	0.268	0.54	0.306	-
Reaction rate coefficient	$k_{0,j,ref} [m^{2.5}/mol^{0.5} s]$	-	$1.764 \cdot 10^{-11}$	-	$3.626 \cdot 10^{-11}$	-
Reference Solid phase Li ⁺ diffusion	$D_{2,j} [m^2/s]$	-	Eq (13)	Eq (13)	Eq (13)	-
Electrolyte phase Li ⁺ diffusion	$D_{1,j,ref} [m^2/s]$	-	$3.9 \cdot 10^{-14}$	-	$1.18 \cdot 10^{-18}$	-
Maximum solid phase concentration	$c_{1,j,max} [mol/m^3]$	-	31,370	-	22,806	-
Initial electrolyte concentration	$c_{2,0}, [mol/m^3]$	-	2000	2000	2000	-
Stoichiometry at 0% SOC	$y_{0\%}, x_{0\%}$	-	0.1	-	0.83	-
Stoichiometry at 100% SOC	$y_{100\%}, x_{100\%}$	-	0.995	-	0.0005	-
Transference Number	t^+	-	-	0.363	-	-
Bruggman tortuosity factor	γ	-	1.5	1.5	1.5	-
Charge transfer coefficient,	α	-	0.5	-	0.5	-
Solid electronic conductivity	$\sigma_{1,j} [S/m]$	$6.63 \cdot 10^{-7}$	100	-	0.5	$3.83 \cdot 10^{-7}$
Ionic conductivity of electrolyte	$\sigma_{2,j} [S/m]$	-	Eq (15)	Eq (15)	Eq (15)	-
Activation energy for reaction	$Ea_{R,j} [J/mol]$	-	$4 \cdot 10^3$	-	$4 \cdot 10^3$	-
Activation energy for particle diffusion	$Ea_{D_{s,j}} [J/mol]$	-	$4 \cdot 10^3$	-	$2 \cdot 10^4$	-
heat capacity	$C_p [J/kg.K]$	385	1437	700	1260	900
density	$\rho [kg/m^3]$	8700	2660	492	1500	2700
thermal conductivity	$\lambda [W/m.K]$	398	1.04	1	1.48	170
Convective heat transfer	$h [W/m^2.K]$	0.03	-	-	-	-
Total number of single cell	N	77	-	-	-	-
Faraday's constant	$F (C/mol)$	96487	-	-	-	-
Reference temperature	$T_{ref} (K)$	298.15	-	-	-	-
Universal gas constant	$R (J/mol.K)$	8.3145	-	-	-	-

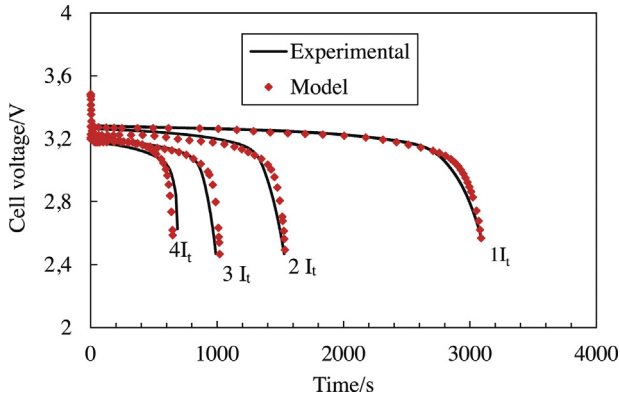


Fig. 5. Comparison between experimental and modeling of cell potential at different discharge current rates.

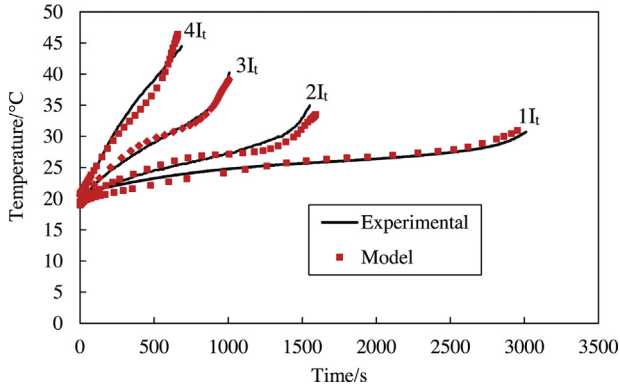


Fig. 6. Comparison between experimental and modeling of the cell maximum temperature at different discharge current rates.

uniform at low current rate (less than $1I_t$) and highly non-uniform at high current rate, where the maximum temperature is located near the positive tab due to the higher resistance of the aluminum. For this reason, the maximum temperatures from the model and the simulation are compared at different discharge current rates in Fig. 6. The simulation results at different discharge rates validate the experimental results. The error varies between 0–2 °C. At high current rates, the battery temperature rises more due to increased heat generation.

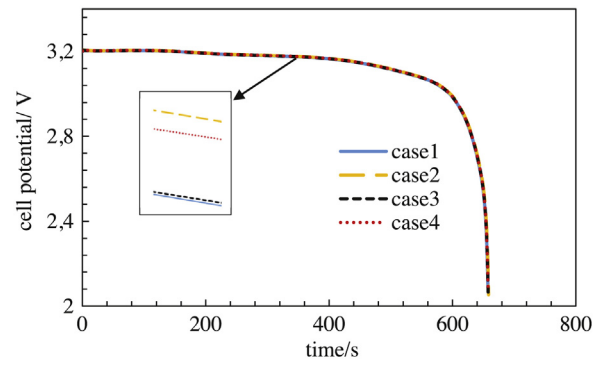


Fig. 7. average cell potential for different cell designs versus time under $4I_t$ discharge rate.

3. Results and discussion

After validation based on case 1, the model is extrapolated to others designs (case 2, case 3 and case 4) with different tab locations as illustrated in Fig. 2. The same current density and physical parameters (electrochemical and thermal) are used for all designs. In order to investigate the impact of cell design on battery behavior, the discharge process under $4I_t$ rate and 20 °C of initial temperature is simulated in adiabatic conditions. In the validation part, convective heat transfer was considered in order to match the experimental conditions.

Fig. 7 shows the average output potential profiles of the different cell designs. The curves have a similar shape, but small potential differences are observed. Case 2 shows less potential drop, followed by case 4, case 3 and case 1. The small differences in potential may be due to the use of cell components with the same dimensions. On the other hand, tab arrangement is responsible for the potential drop by changing the current pathways, which impact the active material utilization. To highlight the origin of the potential drop, potential distributions relative to tab potential along the negative and positive current collector at 640s of discharge time are plotted in Figs. 8 and 9. Regardless of cell design, the potential gradient in both current collectors is mainly localized near the junctions between the tabs and the current collectors. At the beginning of the discharge process, the current enters through the negative tab. Due to resistance and the change of cross-section (between tab and current collector), the current amplitude (represented by the black line) decreases steeply along the flow direction and leads to a

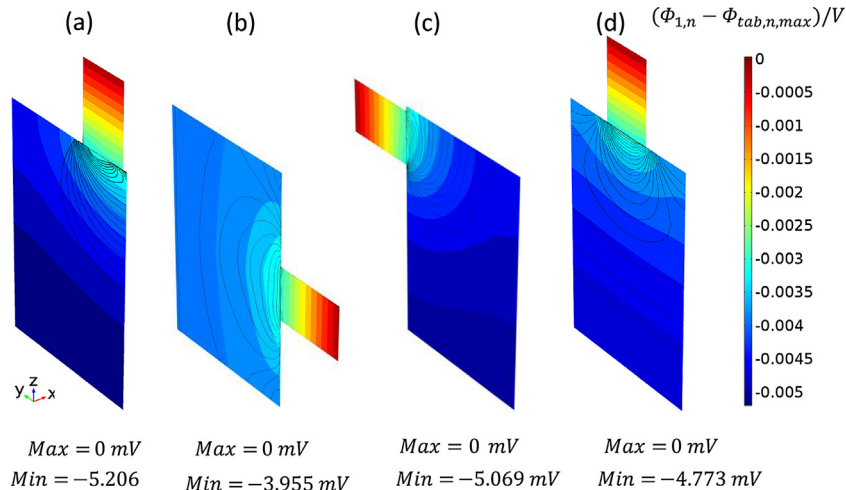


Fig. 8. Potential distribution over the negative current collectors and tab under $4I_t$ discharge rate at 640s for different cell designs: (a) case 1, (b) case 2, (c) case 3 and (d) case 4.

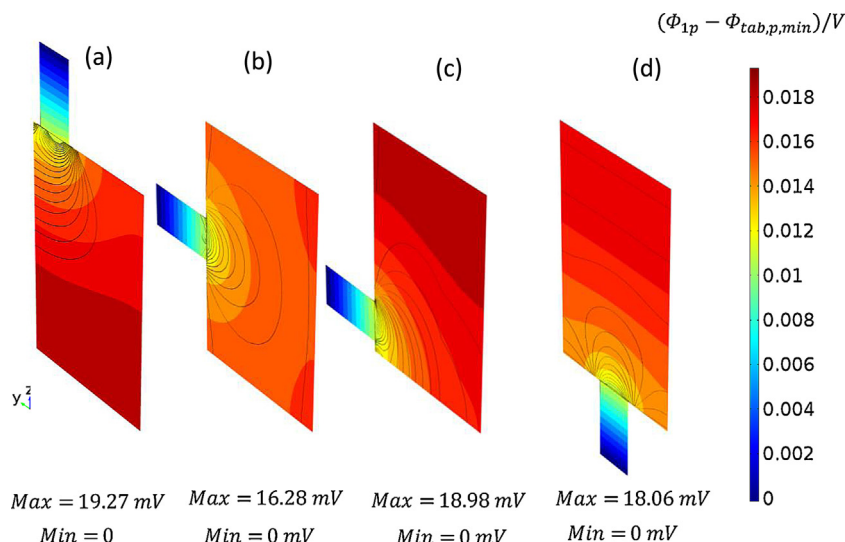


Fig. 9. Potential distribution over the positive current collectors and tabs under $4 I_L$ discharge rate at 640s for different cell designs: (a) case 1, (b) case 2, (c) case 3 and (d) case 4.

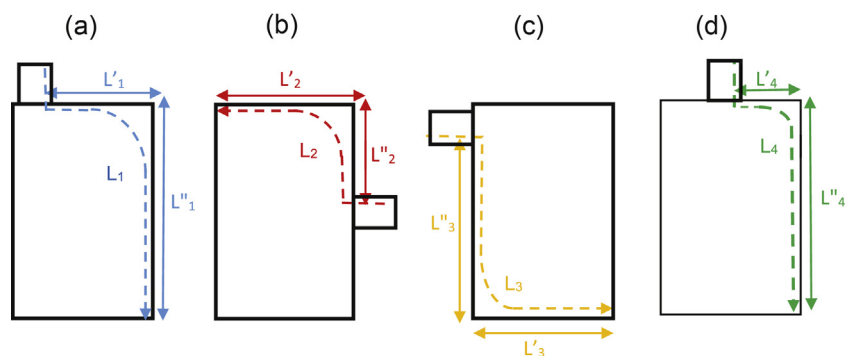


Fig. 10. Maximum current pathway on the negative current collector of different cell designs: (a) case 1, (b) case 2, (c) case 3 and (d) case 4.

gradual potential drop along the negative collector. A similar trend of local overpotential therefore occurs along this current collector. According to the electrochemical kinetics (cf Eq. (7)), the same trend of current density is generated in the positive electrode and then flow out through the positive current collector. Finally, the generated current and the resistance of the Al foil are responsible for the non-uniform potential formed in the positive current collector.

Comparing the different cell designs, case 2 shows the smallest potential gradient, followed by case 4, case 3 and case 1. Due to the positions of their tabs, as described in Fig. 10, L_1 , L_2 , L_3 and L_4 , are proposed to illustrate the maximum current pathways in the current collector of case 1, case 2, case 3 and case 4, respectively. From this figure it is shown that L_2 (~ 240 mm) $< L_4$ (~ 280 mm) $< L_3$ (~ 325 mm) $\leq L_1$ (~ 325 mm). Resistance ($R = (\rho L_i)/S$) of the

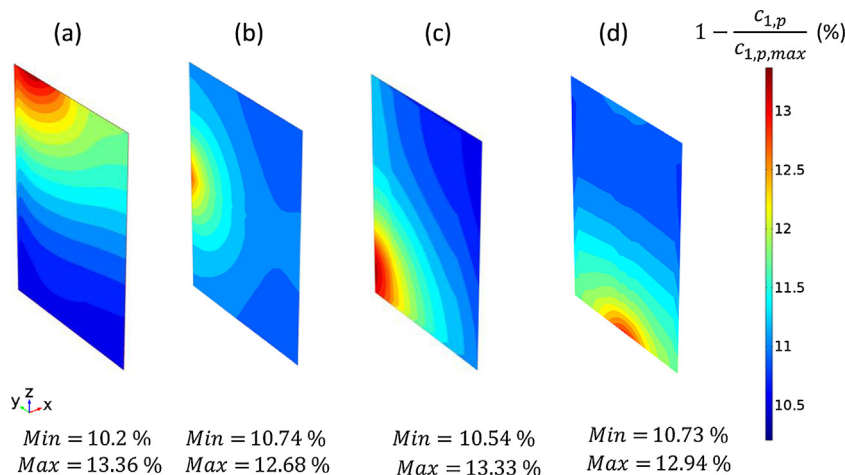


Fig. 11. DoD distribution over the middle of the cathode under $4 I_L$ discharge rate at 640s for different cell designs: (a) case 1, (b) case 2, (c) case 3 and (d) case 4, with $c_{1,p,max}$ the maximum stoichiometric lithium content in the cathode.

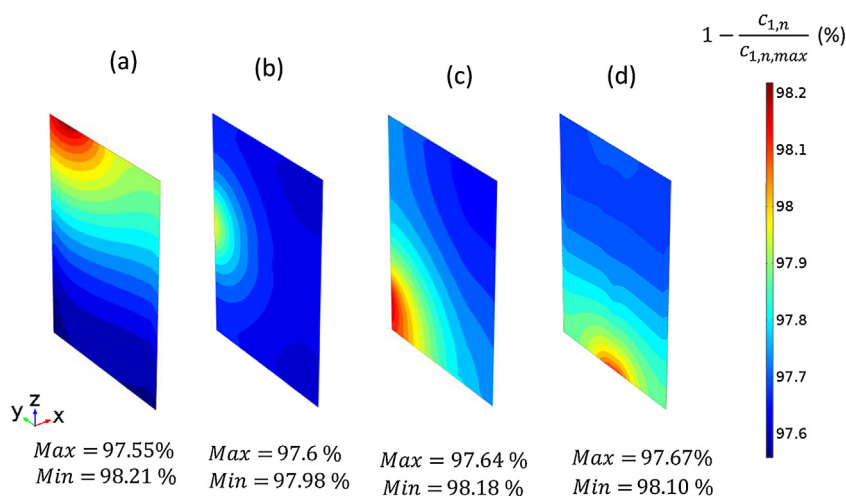


Fig. 12. DoD distribution over the middle of the anode under $4 I_t$ discharge rate at 640s for different cell designs: (a) case 1, (b) case 2, (c) case 3 and (d) case 4, with $c_{1,n,max}$ the maximum stoichiometric lithium content in the anode.

negative current collector is lowest with case 2, which generates the lowest potential gradient. In addition, the voltage drop in case 1 and case 3 are almost the same, due to the same maximum current pathways.

Due to charge conservation, similar trends of current density and potential gradient are generated in the positive current collector, as shown previously. However, the aluminum positive collector has a larger potential gradient due to its high electrical resistivity compared to the copper negative collector. The non-uniform utilization of active material can be quantified by the local depth of discharge (DoD). The DoD distributions along the electrode length are investigated in the different cell designs. Variation of the DoD through the thickness (due to the lithiation/delithiation mechanism) were examined in the literature[10,27,28].

Figs. 11 and 12 show DoD distributions at the middle planes of the anode and cathode. Due to the high local overpotential closer to the positive tabs, the active material in that region is used faster than the rest of the domain and showed higher DoD. As expected, case 2 shows more uniform local DoD compared to other cell designs, due to its uniform local overpotential. This uniform DoD distribution leads to high active material utilization and less potential drop, as observed in Fig. 7.

Regarding thermal behavior, the average temperature of each cell design is represented in Fig. 13. All cell designs have temperature profiles with similar trends, but small differences are observable. These differences may arise from the ohmic heat seen

in Fig. 15, which affects the total heat source (Fig. 16). The high potential gradient drives the increase of ohmic heat (as conductivity multiplied by the gradient of potential squared). As mentioned above, the case 2 design is cycled more uniformly and generates less potential gradient and thus less temperature increase. The same logic can be used to explain the order of temperature increase (Fig. 13) and deviation (Fig. 14) among the different cell designs.

The total heat generation represented in Fig. 16, shows non-linear behavior, with a sharp peak followed by a drop in heat generation near the end of the discharge. To gain better insight into this behavior, different heat contributions (reversible and irreversible) are represented in Fig. 17. It is well known that the reversible heat corresponds to the chemical reaction manifested by an entropy change, while the irreversible heat corresponds to the heat effects of ohmic resistance and polarization. At the beginning of the discharge process, the total heat slightly decreases due to the endothermic reaction (with a negative reversible heat). The contribution of ohmic heat to the irreversible heat is fairly constant throughout the discharge process (cf. Fig. 15). After that, the rapid increase of total heat corresponds to the exothermic reaction (with a positive reversible heat). Near the end of discharge, the rapid increase of total heat is caused by a significant increase in the irreversible heat by polarization heat. Fig. 18 shows the temperature distribution through the different cell designs near the end of the discharge process. It can be seen that each cell design represents comparatively higher temperature near the positive tab (made of aluminum foil) than the rest of the battery, because of the high electrical resistivity and current density in this area. In addition, the

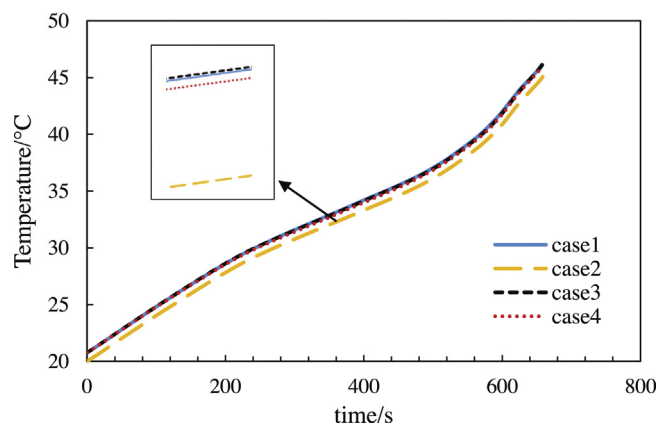


Fig. 13. Comparison of the average temperature under $4 I_t$ discharge rate for the different cell designs.

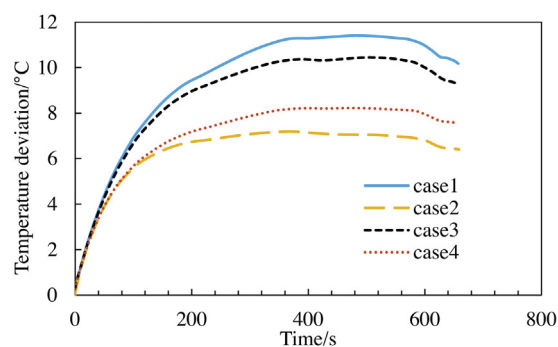


Fig. 14. Comparison of the temperature deviation profiles under $4 I_t$ discharge rate for the different cell designs.

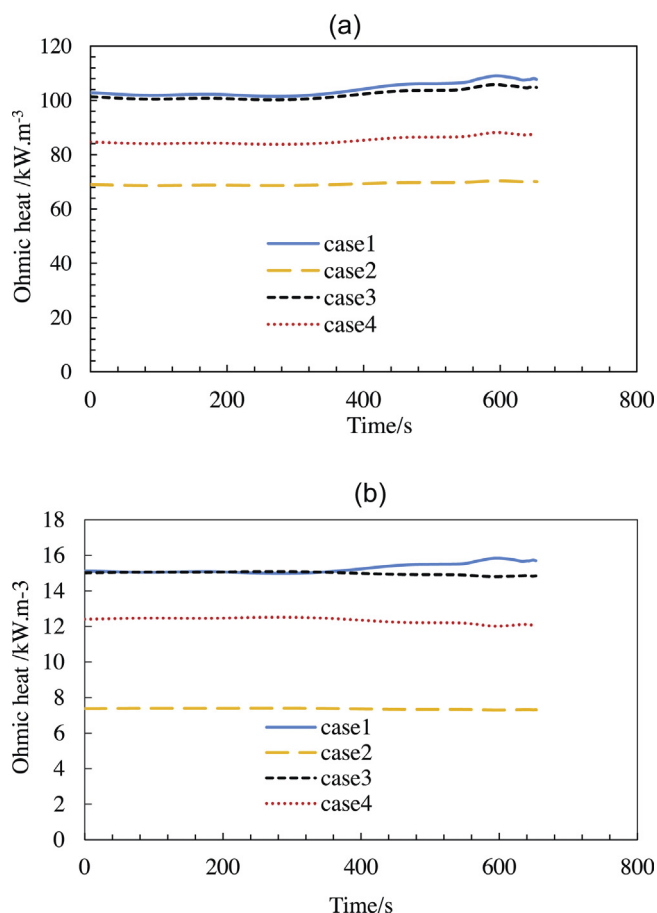


Fig. 15. average ohmic heat sources profiles at (a) the positive current collector and (b) the negative electrode under 4 I_t discharge rate.

temperature gradient is lower with cases 2 and case 4 due to the uniform potential and current distributions observed previously, which lead to lower heat source gradients. Uniform temperature distribution over the surface could be obtained by balancing the tab widths.

In summary, the statistical distributions of temperature, potential and current density are represented in Fig. 19. Distributions are computed from the difference between the maximum and the

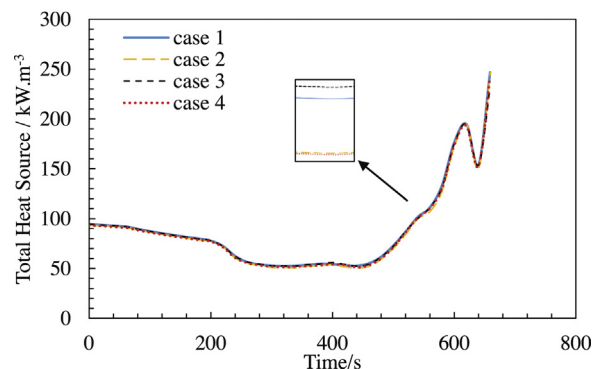


Fig. 16. Comparison of the average heat sources profiles under 4 I_t discharge rate for the different cell design.

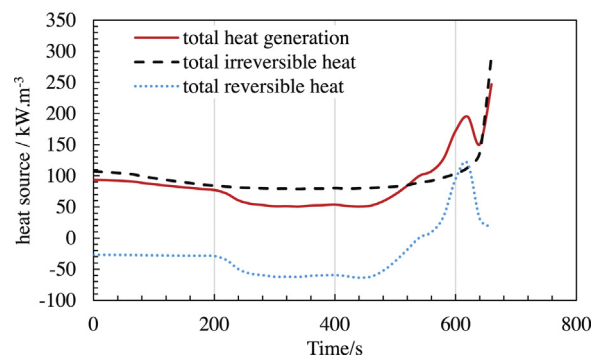


Fig. 17. total, reversible and irreversible heat sources under 4 I_t discharge rate for case 2 cell design.

minimum, and normalized by the maximum distribution obtained between the different cases ($\Delta M = \frac{\max(M_{\max} - M_{\min})}{\max_{\text{cases}}(M_{\max} - M_{\min})}$), where M

stands for the temperature, current density and potential. It is shown that case 2 and case 4 present more uniform temperature, potential and current distributions due to symmetrical arrangement of their tabs (placed at the center of the cell), which minimize the maximum current pathways. At pack level, the battery design based on case 2 can be cycled more uniformly, requiring a less complex cooling system and strategy.

As case 2 presents the most favorable cell design in term of thermal, voltage and current distributions, in-depth investigations are

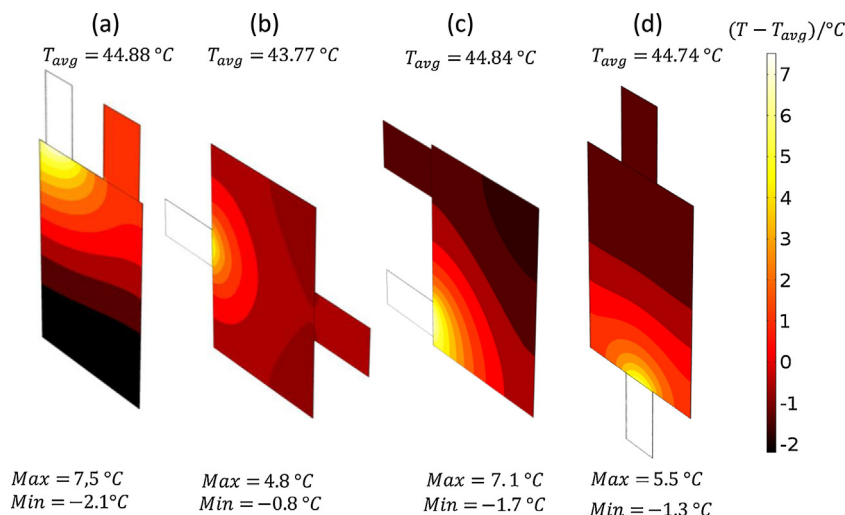


Fig. 18. Temperature distribution over the cell under 4 I_t discharge rate at 640s for different cell designs: (a) case 1, (b) case 2, (c) case 3 and (d) case 4.

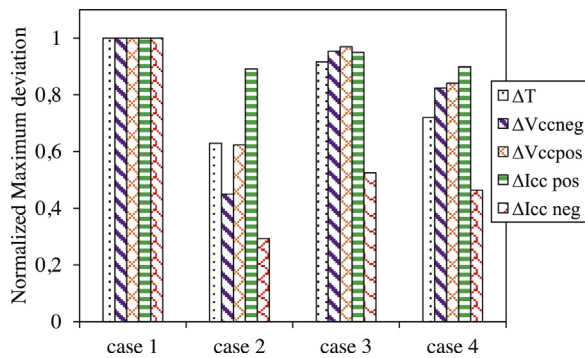


Fig. 19. Summary of Comparison between cell designs under 4 I_t discharge rate.

Table 5

Value of investigated tab widths of the case 2 design.

	1* L _{tab}	2* L _{tab}	3* L _{tab}	4* L _{tab}
Positive tab (m)	0.04	0.08	0.12	0.16
negative tab(m)	0.05	0.10	0.15	0.25

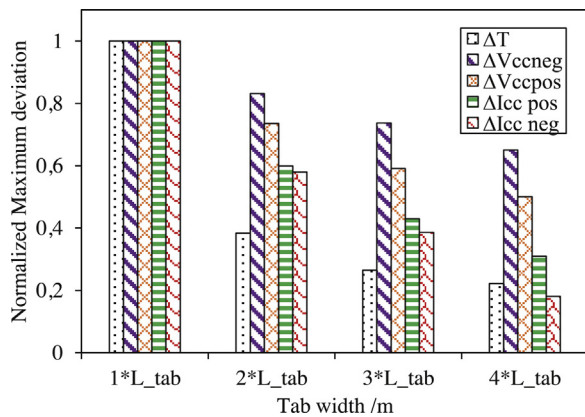


Fig. 20. Influence of the tab width on the distribution under 4 I_t discharge rate L_{nc}.

carried out with this case in order to highlight the impact of the tab width on the distribution. The values of the tab width investigated are summarized in Table 5. As shown in Fig. 20, the temperature, potential and current density distributions become more uniform with the increase of tab width, because current density decreases as the surface increases. An increase of tab width gives more uniform potential, current density and thermal distributions, leading to uniform utilization of the active material, which tends to improve battery performance by increasing the output voltage and capacity of the cell. It also tends to increase energy and power densities as established in the literature [10,29].

4. Conclusion

Extensive three-dimensional simulations of large LiFePO₄ pouch cells have been carried out to investigate the impact of different pouch cell designs on performance and variable distributions. It has been shown that the cell designs with symmetrical configurations

(case 2 and case 4) show uniform potential and current density gradient, which minimize the ohmic heat and lead to more uniform active material utilization and temperature distributions across the cell surface. Cell design with symmetrical configuration tends to minimize the maximum current pathways. It is found that the high potential, current density and temperature gradient are mainly located near the positive tab due to its high resistivity. Due to charge conservation, the potential distribution along the negative current collector at the beginning of discharge are responsible for the non-uniform active material utilization and the potential distribution in the positive current collector. In addition, the increase of the tab width makes the potential, current density and thermal distributions more uniform and improve the battery performance by increasing its output voltage. This also tends to increase the energy and power densities. At the pack level, the design of case 2 with subsequent tab width can be cycled more uniformly and thereby allows a less complex cooling strategy.

References

- [1] P. Van den Bossche, F. Vergels, J. Van Mierlo, J. Matheys, W. Van Autenboer, *Journal of Power Sources* 162 (2006) 913.
- [2] J. Axsen, K.S. Kurani, A. Burke, *Transport Policy* 17 (2010) 173.
- [3] J.V.M. P. Van den Bossche, N. Omar, M. Al Sakka, A. Samba, H. Gualous, In: G. Pistoia (Ed.), Elsevier, Amsterdam, 2014, 249–271.
- [4] N. Omar, M.A. Monem, Y. Firouz, J. Salminen, J. Smekens, O. Hegazy, H. Gualous, G. Mulder, P. Van den Bossche, T. Coosemans, J. Van Mierlo, *Applied Energy* 113 (2014) 1575.
- [5] N. Omar, H. Gualous, J. Salminen, G. Mulder, A. Samba, Y. Firouz, M.A. Monem, P. Bossche, J. Mierlo, *Journal of Applied Electrochemistry* (2013).
- [6] A. Barré, B. Deguilhem, S. Grolleau, M. Gérard, F. Suard, D. Riu, *Journal of Power Sources* 241 (2013) 680.
- [7] Q. Wang, P. Ping, X. Zhao, G. Chu, J. Sun, C. Chen, *Journal of Power Sources* 208 (2012) 210.
- [8] C.-Y. Jhu, Y.-W. Wang, C.-M. Shu, J.-C. Chang, H.-C. Wu, *Journal of Hazardous Materials* 192 (2011) 99.
- [9] G.-H. Kim, A. Pesaran, R. Spotnitz, *Journal of Power Sources* 170 (2007) 476.
- [10] W. Zhao, G. Luo, C.-Y. Wang, *Journal of Power Sources* 257 (2014) 70.
- [11] K.-J. Lee, K. Smith, A. Pesaran, G.-H. Kim, *Journal of Power Sources* 241 (2013) 20.
- [12] U.S. Kim, C.B. Shin, C.-S. Kim, *Journal of Power Sources* 180 (2008) 909.
- [13] U.S. Kim, C.B. Shin, C.-S. Kim, *Journal of Power Sources* 189 (2009) 841.
- [14] J.E. Soc, J. The, E. Society, P.A. Flowers, G. Mamantov, T. Journal, J.H. Taylor, W.S. Benedict, J. Strong, J. Chem, M. Doyle, T.F. Fuller, J. Newman 140 (1993) 1526.
- [15] P.M. Gomadam, J.W. Weidner, R.A. Dougal, R.E. White, *Journal of Power Sources* 110 (2002) 267.
- [16] W.B. Gu, C.Y. Wang, *Journal of The Electrochemical Society* 147 (2000) 2910.
- [17] V. Srinivasan, C.Y. Wang, *Journal of The Electrochemical Society* 150 (2003) A98.
- [18] M. Xu, Z. Zhang, X. Wang, L. Jia, L. Yang, *Journal of Power Sources* 256 (2014) 233.
- [19] M. Guo, G.-H. Kim, R.E. White, *Journal of Power Sources* 240 (2013) 80.
- [20] M. Guo, R.E. White, *Journal of Power Sources* 221 (2013) 334.
- [21] S. Tippmann, D. Walper, L. Balboa, B. Spier, W.G. Bessler, *Journal of Power Sources* 252 (2014) 305.
- [22] X. Li, M. Xiao, S.-Y. Choe, *Electrochimica Acta* 97 (2013) 66.
- [23] L.H. Saw, Y. Ye, A.A.O. Tay, *Energy Conversion and Management* 75 (2013) 162.
- [24] L.H. Saw, K. Somasundaram, Y. Ye, A.A.O. Tay, *Journal of Power Sources* 249 (2014) 231.
- [25] A. Samba, N. Omar, H. Gualous, Y. Firouz, P. Van den Bossche, J. Van Mierlo, T.I. Boubekeur, *Electrochimica Acta* 117 (2014) 246.
- [26] A. Samba, H. Louahlia-Gualous, S. Le Masson, D. Nörterhäuser, *Applied Thermal Engineering* 50 (2013) 1351.
- [27] K. Somasundaram, E. Birgersson, A. Sadashiv, *Journal of Power Sources* 203 (2012) 84.
- [28] J. Li, Y. Cheng, M. Jia, Y. Tang, Y. Lin, Z. Zhang, Y. Liu, *Journal of Power Sources* 255 (2014) 130.
- [29] K.-J. Lee, K. Smith, A. Pesaran, G.-H. Kim, *Journal of Power Sources* 241 (2013) 20.